





# The dusty red supergiant progenitor and the local environment of the Type II SN 2023ixf in M101

ZEXI NIU <sup>1,2</sup> NING-CHEN SUN <sup>1,2</sup> JUSTYN R. MAUND <sup>3</sup> YU ZHANG <sup>4</sup> RUINING ZHAO <sup>1,2</sup> AND  
JIFENG LIU<sup>5,1,6</sup>

<sup>1</sup>*School of Astronomy and Space Science, University of Chinese Academy of Sciences, Beijing 100049, People's Republic of China*

<sup>2</sup>*National Astronomical Observatories, Chinese Academy of Sciences, 20A Datun Road, Chaoyang District, Beijing, China*

<sup>3</sup>*Department of Physics and Astronomy, University of Sheffield, Hicks Building, Hounsfield Road, Sheffield, S3 7RH, United Kingdom*

<sup>4</sup>*Key Laboratory of Optical Astronomy, National Astronomical Observatories, Chinese Academy of Sciences, Beijing 100101, China*

<sup>5</sup>*New Cornerstone Science Laboratory, National Astronomical Observatories, Chinese Academy of Sciences, Beijing 100012, People's Republic of China*

<sup>6</sup>*Institute for Frontiers in Astronomy and Astrophysics, Beijing Normal University, Beijing, 102206, People's Republic of China*

## ABSTRACT

As one of the closest supernovae (SNe) in the last decade, SN 2023ixf is an unprecedented target to investigate the progenitor star that exploded. However, there is still significant uncertainty in the reported progenitor properties. In this work, we present a detailed study of SN 2023ixf's progenitor with two independent analyses. We first modelled its spectral energy distribution (SED) based on Hubble Space Telescope optical, Spitzer mid-infrared (IR), and ground-based near-IR data. We find that stellar pulsation and circumstellar extinction have great impacts on SED fitting, and the result suggests a relatively massive red supergiant (RSG) surrounded by C-rich dust with an initial mass of 16.2–17.4  $M_{\odot}$ . The corresponding mass-loss rate estimate is  $1 \times 10^{-5} M_{\odot}/\text{yr}$ . We also derived the star formation history of the SN environment based on resolved stellar populations, and the most recent star-forming epoch corresponds to a progenitor initial mass of 17–19  $M_{\odot}$ , in agreement with that from our SED fitting. Therefore, we conclude that the progenitor of SN 2023ixf is close to the high-mass end for Type II SN progenitors.

## 1. INTRODUCTION

Core-collapse supernovae (SNe) are the spectacular explosions of dying massive ( $>8 M_{\odot}$ ) stars. It is a major goal, and currently a major difficulty, to determine the progenitor stars of different SN types. It has been confirmed that the Type II-P SNe arise from the explosion of red supergiants (RSGs) with almost 20 directly probed progenitors (e.g. SN 2003gd, Smartt et al. 2004; Maund & Smartt 2009; SN 2005cs, Maund et al. 2005; SN 2017eaw, Van Dyk et al. 2019; Rui et al. 2019). However, none of them appear more massive than  $\sim 16$ – $18 M_{\odot}$ , which is significantly lower than the theoretically predicted upper mass limit of 25–30  $M_{\odot}$  (i.e. the “RSG problem”; Smartt 2009, 2015; although see also Davies & Beasor 2018). This could be due to the very uncertain circumstellar extinction, which may lead to underestimation of the progenitor masses (Walmswell & Eldridge 2012); it is also possible that the more massive

stars may explode as other types of SNe (e.g. Type II-L or Type II<sub>n</sub>; Groh et al. 2013) or even collapse directly into a black hole (Sukhbold et al. 2016).

Compared with Type II-P SNe, Type II-L SNe have no significant plateau phase in their light curves since their progenitors only retain a low-mass (1–5  $M_{\odot}$ ) H envelope before explosion (Swartz et al. 1991). It is possible that their progenitors are more massive than the Type II-P SN progenitors and thus are more significantly stripped by their intense stellar wind (Faran et al. 2014). It is also poorly understood whether interacting binaries, which have already been known to produce many stripped-envelope SN types (e.g. IIb, Ib, Ic and Ibn; Maund et al. 2004; Eldridge et al. 2013; Fang et al. 2019; Sun et al. 2020a,b, 2022, 2023a), could also be responsible for the Type II-L SNe. With very few directly detected progenitors (e.g. SN 2009kr; Elias-Rosa et al. 2010, although see Maund et al. 2015), the origin of Type II-L SNe is still an unresolved mystery.

SN 2023ixf is a Type II SN that recently exploded in the nearby galaxy M101 (i.e. the Whirlpool galaxy; Itagaki 2023). Its early spectra show prominent and

narrow nebular emission lines, suggesting the presence of circumstellar material (CSM) around the progenitor (Yamanaka et al. 2023; Smith et al. 2023; Vasylyev et al. 2023; Teja et al. 2023; Jacobson-Galan et al. 2023; Hiramatsu et al. 2023). Soon after the explosion, several groups reported the detection of a progenitor candidate for SN 2023ixf on pre-explosion images (e.g. Pledger & Shara 2023; Kilpatrick et al. 2023; Jencson et al. 2023; Soraisam et al. 2023). Their results are all consistent with a RSG progenitor enshrouded by a dusty envelope. The inferred progenitor mass is, however, still under debate and can range from 8–10  $M_{\odot}$  up to  $\sim 20 M_{\odot}$ . This large uncertainty presents a significant challenge to further studies of SN 2023ixf.

In this paper, we carry out a detailed analysis of the progenitor of SN 2023ixf in order to derive its accurate properties. We use two different techniques, based on the direct progenitor detection and SN environment, to assess the reliability of our results against possible systematic errors. Throughout this paper, we adopt a distance of  $6.85 \pm 0.15$  Mpc (Riess et al. 2022), a Milky Way extinction of  $E(B - V)_{\text{MW}} = 0.008$  mag (Schlafly & Finkbeiner 2011), a host galaxy extinction of  $E(B - V)_{\text{host}} = 0.033$  (Lundquist et al. 2023; Smith et al. 2023; Jacobson-Galan et al. 2023), and a standard extinction law with  $R_V = 3.1$  (Cardelli et al. 1989). All magnitudes are reported in the Vega system unless otherwise specified.

## 2. DATA AND PHOTOMETRY

### 2.1. *HST* optical data

The site of SN 2023ixf was observed by Hubble Space Telescope (HST) with the Wide Field and Planetary Camera 2 (WFPC2), the Wide Field Camera 3 (WFC3), and the Advanced Camera for Surveys (ACS) before explosion. We retrieved the calibrated images from the Mikulski Archive for Space Telescopes<sup>1</sup> and reprocessed them with the ASTRODRIZZLE package (Gonzaga et al. 2012) for better image alignment and cosmic ray removal. On the ACS F814W image, there are two objects within 0.2 arcsec from the reported SN position and Kilpatrick et al. (2023) identified the relatively brighter one as the SN progenitor (Fig. 1) based on differential astrometry with post-explosion images. We performed point-spread-function (PSF) photometry with the DOLPHOT package (Dolphin 2000) and detected the progenitor significantly in the F658N, F675W, and F814W bands. The measured magnitudes, which are listed in Table 1, are slightly brighter than those re-

ported by Kilpatrick et al. (2023) within 1–4 $\sigma$  uncertainties (note their magnitudes are in the AB system). The difference could be due to our different parameters in DOLPHOT photometry, and this difference does not have any significant effect in the following analysis. The progenitor was not detected in any other bands, and we estimated the detection limits with artificial star tests. We also used the ACS F435W, F555W, and F814W photometry to perform an environmental analysis of the resolved stellar populations around SN 2023ixf (Section 4.2).

**Table 1.** HST observations used in this work and photometry of SN 2023ixf’s progenitor. The other HST observations are not listed since their detection limits are not very constraining for the progenitor’s SED (Section 3) or because they are not used in the environmental analysis (Section 4.2).

Epoch (MJD)	Program ID	Instrument and filter	Magnitude
52593.99	9490 <sup>a</sup>	ACS/F435W	> 27.3
52594.01	9490	ACS/F555W	> 27.0
53045.01	9720 <sup>b</sup>	ACS/F658N	24.75 (0.20)
51261.04	6829 <sup>c</sup>	WFPC2/F675W	25.36 (0.19)
52594.02	9490	ACS/F814W	24.34 (0.05)

PIs: (a) K. Kuntz; (b) P. Chandar; (c) Y.-H. Chu.

### 2.2. *Spitzer* mid-IR data

The site of SN 2023ixf was observed by Spitzer/IRAC at a total of 31 epochs during its cold mission in 2004 and during the warm mission in 2012–2019. We retrieved the post-basic calibrated (PBCD) images from the Spitzer Heritage Archive<sup>2</sup>, and a pre-explosion source is clearly visible at the SN position in the [3.5] and [4.5] bands (Fig. 1). We used the DOPHOT package (Schechter et al. 1993) to perform PSF photometry at individual epochs, the results of which are listed in Table 2 and displayed in Fig. 2. Prominent variability, with a semi-amplitude of  $\sim 0.25$  mag, can be seen in both the [3.6] and [4.5] bands without obvious color variation. This variability is significant compared with the photometric uncertainties and not due to the possible zero-point shift between different epochs (using non-variable field stars to provide a reference, we found the zero-point shift, if any, to be negligible compared with the progenitor’s variability). This variability was also reported in Kilpatrick et al. (2023), Jencson et al. (2023), and Soraisam et al. (2023), and they all found a pulsational period of  $\sim 1000$  days. We derived phase-weighted average magnitudes of

<sup>1</sup> <https://archive.stsci.edu>

<sup>2</sup> <https://sha.ipac.caltech.edu>

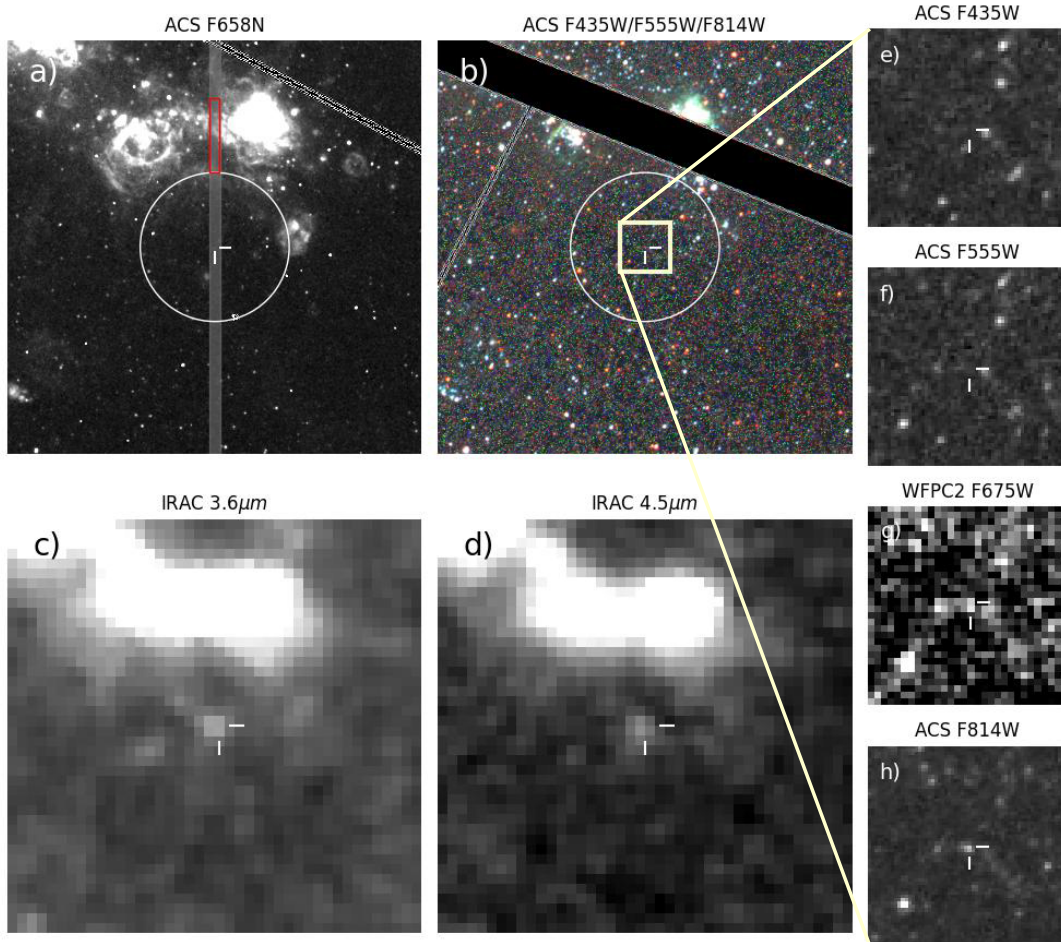


**Figure 1.** (a, b) HST and (c, d) Spitzer images of the site of SN 2023ixf. The SN position is shown by the cross-hair and the images have a dimension of  $25 \text{ arcsec} \times 25 \text{ arcsec}$ . In the F658N narrow-band image (a), a few H II regions are visible to the west and to the north of SN 2023ixf, and the grey-shaded stripe shows the slit position in one of our long-slit spectroscopic observations of the SN (Zhang et al. in preparation); we extracted a spectrum from the red-outlined area in order to estimate the metallicity of the ionized gas (Section 4.1). In (a) and (b), the circle is centered at the SN position with a radius of 150 pc, within which we selected stars for an environmental analysis (Section 4.2). (e-h) Stamps of HST images in the F435W, F555W, F675W, and F814W bands, all with a dimension of  $3 \text{ arcsec} \times 3 \text{ arcsec}$ . All panels are aligned North up and East to the left.

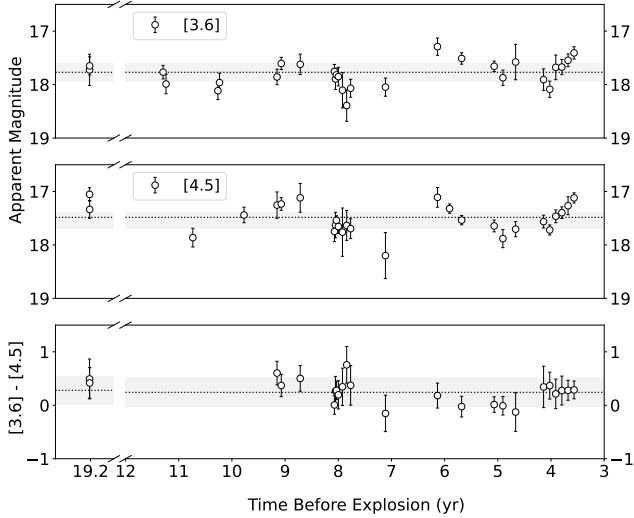


**Figure 2.** Light and color curves of the progenitor of SN 2023ixf. The dotted horizontal lines are the phase-weighted averages and the light-shaded regions reflect the typical photometric uncertainties.

$[3.6] = 17.78 \pm 0.19$  mag and  $[4.5] = 17.50 \pm 0.20$  mag. On the [5.8] and [8.0] images, however, no counterpart can be significantly detected at the SN position down to  $3\sigma$  detection limits of 14.95 and 14.38 mag, respectively.

### 2.3. Ground-based near-IR data

During the writing of this paper, Soraisam et al. (2023) reported *JHK*-band light curves acquired from the Gemini Near-IR Imager (NIRI) and the Wide Field Camera (WFCAM) on the United Kingdom Infrared Telescope (UKIRT) images. Their photometry is roughly consistent with those derived by Jencson et al. (2023) and Kilpatrick et al. (2023) based on observations with NIRI, NEWFIRM infrared camera, and/or the Magellan Infrared Spectrograph (MMIRS). In this paper, we applied *JHK*-band photometry of Soraisam et al. (2023) and computed the phase-weighted average  $J = 20.67 \pm 0.19$  mag,  $H = 19.55 \pm 0.13$  mag, and  $K = 18.69 \pm 0.08$  mag with their period and amplitudes, since their data have better phase coverage.

## 3. SED ANALYSIS

### 3.1. Method

RSGs could experience significant mass loss and enshroud themselves within dusty envelopes (de Jager et al. 1988; van Loon et al. 2005a; Massey et al. 2005; Beasor et al. 2020). The uncertain circumstellar extinction often leads to an underestimation of the progenitor mass based on detections in only one or a few filters (e.g.

**Table 2.** Spitzer/IRAC photometry of the progenitor of SN 2023ixf in the [3.6] and [4.5] bands.

Epoch (MJD)	[3.6] (mag)	[4.5] (mag)
53072.09	17.73 (0.29)	17.05 (0.12)
53072.49	17.65 (0.17)	17.34 (0.17)
55960.72	17.77 (0.13)	–
55980.99	17.99 (0.18)	–
56165.01	–	17.86 (0.17)
56337.07	18.12 (0.17)	–
56348.11	17.96 (0.17)	–
56516.35	–	17.44 (0.15)
56742.84	17.86 (0.15)	17.25 (0.25)
56771.83	17.60 (0.11)	17.23 (0.12)
56902.01	17.62 (0.19)	17.12 (0.27)
57136.69	17.75 (0.13)	17.75 (0.19)
57144.06	17.89 (0.20)	17.63 (0.24)
57150.17	17.82 (0.11)	17.54 (0.09)
57163.71	17.85 (0.17)	17.66 (0.13)
57191.82	18.11 (0.33)	17.76 (0.45)
57220.79	18.39 (0.29)	17.64 (0.28)
57247.82	18.07 (0.17)	17.70 (0.19)
57486.85	18.05 (0.17)	18.20 (0.43)
57843.93	17.29 (0.16)	17.11 (0.18)
57926.90	–	17.32 (0.09)
58009.67	17.51 (0.11)	17.54 (0.09)
58232.95	17.66 (0.10)	17.64 (0.11)
58292.87	17.87 (0.14)	17.88 (0.17)
58380.22	17.58 (0.33)	17.70 (0.14)
58572.08	17.91 (0.20)	17.56 (0.12)
58614.39	18.09 (0.15)	17.72 (0.09)
58655.68	17.68 (0.23)	17.46 (0.12)
58697.50	17.67 (0.14)	17.40 (0.11)
58740.01	17.55 (0.12)	17.27 (0.17)
58781.31	17.41 (0.12)	17.12 (0.09)
phase-weighted average	17.78 (0.19)	17.50 (0.20)

Van Dyk et al. 2019). For the progenitor of SN 2023ixf, however, the extensive optical, near-IR and mid-IR data allow us to perform a detailed modeling of its spectral energy distribution (SED).

The intrinsic SED of the SN progenitor was synthesized by the MARCS model atmospheres (Gustafsson et al. 2008), assuming a microturbulent velocity of  $5 \text{ km s}^{-1}$ , surface gravity  $\log(g) = 0$  dex and metallicity  $[\text{Fe}/\text{H}] = -0.25$  dex (close to our estimation in Section 4.1). For the effective temperature, we tried three different values of  $T_{\text{eff}} = 3400, 3700, \text{ and } 4000 \text{ K}$ , which are typical of RSGs. The radiation transfer through the

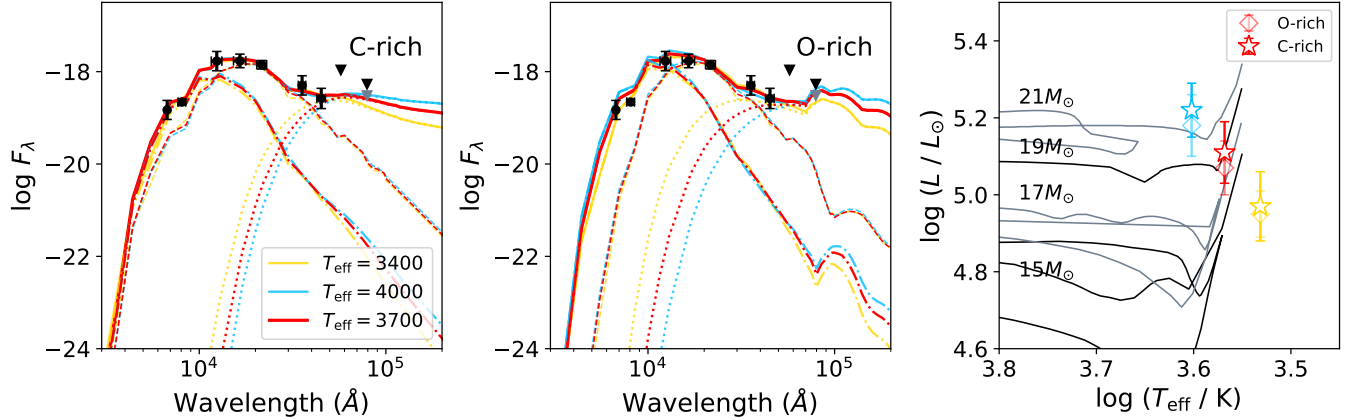


**Figure 3.** (a) Observed SED (black data points) and the best-fitting model with C-rich dust (colored solid lines) for the progenitor of SN 2023ixf. The vertical error bars reflect their  $3\sigma$  photometric uncertainties and the horizontal error bars are the root-mean-square bandwidths. Only  $3\sigma$  detection limits in Spitzer/IRAC [5.8] and [8.0] bands are displayed (inverted triangles), and those in the other bands are not very constraining on the progenitor’s SED. The  $2\sigma$  detection limit in [8.0] band is shown in gray. The dashed, dotted, and dot-dashed lines correspond to the attenuated RSG radiation, dust emission, and dust-scattered radiation, respectively. The yellow, red, and blue colors correspond to effective temperatures of  $T_{\text{eff}} = 3400$ ,  $3700$ , and  $4000$  K for the RSG progenitor. Detailed model parameters are listed in Table 3. (b) Same as (a) but for the O-rich dust model. Notice that the prominent silicate bumps of  $T_{\text{eff}} = 3700$  and  $4000$  K models almost exceed the [8.0] detection limit. (c) The progenitor of SN 2023ixf on the Hertzsprung-Russell diagram. The diamonds and stars demonstrate models with O-rich and C-rich dust, respectively. They are colored in the same way as (a-b). Overlaid black/grey lines are the PARSEC stellar evolutionary tracks for different initial masses.

**Table 3.** Best-fitting and derived parameters of the SED for the progenitor of SN 2023ixf .

	$T_{\text{eff}}$ (K)	$\log(L/L_{\odot})$	$T_{\text{in}}$ (K)	$\tau_V$	$E(B - V)_{\text{CSM}}$ (mag)	Comment
C-rich	3400	$4.97^{+0.09}_{-0.08}$	$514^{+96}_{-70}$	$5.37^{+0.64}_{-0.59}$	1.39	
	3700	$5.11^{+0.08}_{-0.08}$	$433^{+55}_{-50}$	$6.39^{+0.58}_{-0.59}$	1.64	(a)
	4000	$5.22^{+0.07}_{-0.08}$	$387^{+46}_{-39}$	$7.16^{+0.54}_{-0.53}$	1.85	
O-rich	3400	$4.95^{+0.06}_{-0.05}$	$1025^{+317}_{-283}$	$12.13^{+0.86}_{-0.93}$	1.88	
	3700	$5.07^{+0.08}_{-0.06}$	$715^{+337}_{-208}$	$12.79^{+0.94}_{-0.93}$	1.98	(b)
	4000	$5.18^{+0.09}_{-0.05}$	$553^{+272}_{-298}$	$13.15^{+1.01}_{-0.91}$	2.04	(b)

Comments: (a) This is the most favored effective temperature since the other temperatures are either too cold or too warm compared with that of a RSG just before the explosion (Fig. 3c). (b) These two models have prominent silicate bumps that almost exceed the [8.0] detection limits.

dusty envelope was then solved with the DUSTY code. We used a  $\rho \propto r^{-2}$  wind-like radial density profile and the default relative shell thickness that is 1000 times the inner radius. The standard Mathis, Rumpl & Nordsieck (1977; MRN) grain size distribution (Mathis et al. 1977) was adopted, and we considered two different types of dust grains made of either pure graphite or pure silicate (Draine & Lee 1984), representing a C-rich or O-rich chemical composition, respectively. The progenitor’s bolometric luminosity,  $L_{\text{bol}}$ , the dust temperature at the inner shell boundary,  $T_{\text{in}}$  (which is required to be lower than 1500 K such that the dust can survive in the envelope; Pozzo et al. 2004; Sarangi et al. 2018), and the V-band optical depth of the envelope,  $\tau_V$ , were left as free parameters to be fitted from the data.

We used the Markov Chain Monte Carlo method to search for models that match the progenitor detections in the F675W, F814W, J, H, K, [3.6], and [4.5] filters. We used the phase-weighted average magnitudes for the near- and mid-IR filters; for the optical F675W and F814W filters, however, data at only one epoch are available and it is difficult to estimate their phase-weighted average magnitudes. Therefore, in these two filters, we conservatively allowed the model magnitudes to vary within 0.5 mag from the observed ones, accounting for their possible variability due to stellar pulsation (see Section 5 for a more detailed discussion).

### 3.2. Results

The best-fitting model SED with C-rich/O-rich dust and with different progenitor effective temperatures are displayed in Fig. 3 (a, b), and the detailed parameters are listed in Table 3. The circumstellar extinction  $E(B - V)_{\text{CSM}}$  is also computed according to the equation in Kochanek et al. (2012) and convolved with the passbands. Note, however, the O-rich models with  $T_{\text{eff}} = 3700$  and 4000 K have prominent silicate bumps that almost exceed the  $3\sigma$  [8.0] detection limit, and significantly exceed the limit at the  $2\sigma$  level (15.0 mag). Therefore, there is a 95% probability that these two models are against the observations.

The position of SN 2023ixf’s progenitor on the Hertzsprung-Russell diagram is shown in Fig. 3c in comparison with the PARSEC v1.2S single-star evolutionary tracks (Bressan et al. 2012). Although we tried 3 different effective temperatures typical of RSGs, only the intermediate value (i.e.  $T_{\text{eff}} = 3700$  K) is consistent with the end points of the tracks, while the other two values (3400 and 4000 K) are either too cold or too warm for a RSG just before the explosion (we note, however, there could be uncertainties in the estimate and model prediction of the effective temperature of RSGs; e.g. Davies

et al. 2013.) Therefore, assuming single-star evolution SN 2023ixf is most likely to have a relatively massive progenitor with  $M_{\text{ini}} = 16.2\text{--}17.4 M_{\odot}$  enshrouded by a C-rich dusty envelope.

Given properties of CSM, the mass-loss rate ( $\dot{M}$ ) can be calculated following  $\dot{M} = \frac{16\pi}{3} \frac{R_{\text{in}} \tau_V \rho_d a V_{\text{exp}}}{Q} r_{\text{gd}}$  (Beasor & Davies 2016), where  $V_{\text{exp}} = 25$  km/s is expansion velocity,  $r_{\text{gd}} = 400$  is gas to dust ratio considering a half-solar metallicity (van Loon et al. 2005b),  $Q_V = 0.4$  is effective extinction efficiency,  $a = \sqrt{0.005 \times 0.25} \mu\text{m}$  is grain size,  $r_{\text{gd}} = 2.26$  g/cm<sup>3</sup> is grain bulk density (Draine & Lee 1984). We have  $\dot{M} \approx 1 \times 10^{-5} M_{\odot}/\text{yr}$ . In another hand, Beasor et al. (2020) (also see their Erratum Beasor et al. 2023) established empirical mass-dependent  $\dot{M}$ - $L_{\text{bol}}$  relation based on the Galactic RSGs and RSGs in LMC which are in the earlier evolutionary stages. Assuming  $M_{\text{ini}} = 17 M_{\odot}$  and  $L_{\text{bol}} = 5.11^{+0.08}_{-0.08}$ , the implied mass-loss rate is  $1\text{--}4 \times 10^{-6} M_{\odot}/\text{yr}$ , which is smaller than that derived by the CSM directly. It tells that the progenitor of SN 2023ixf might experienced an enhanced mass-loss  $\sim 20\text{--}3$  yr before the explosion.

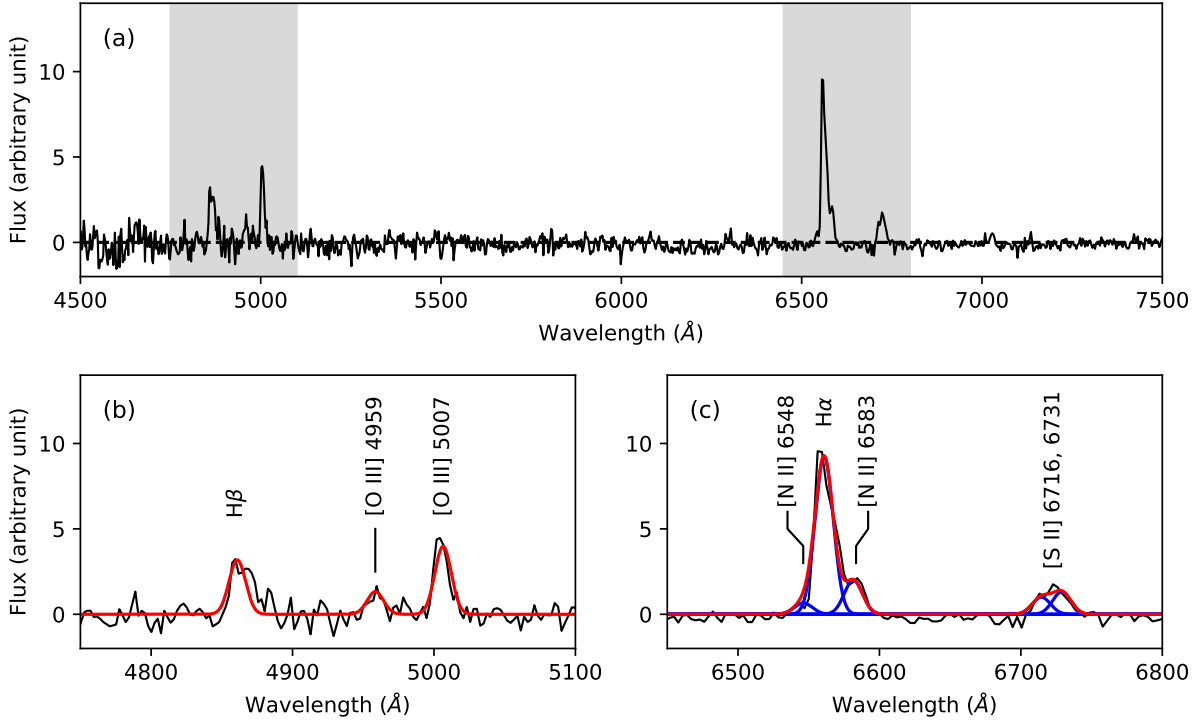
## 4. ENVIRONMENTAL ANALYSIS

### 4.1. Metallicity

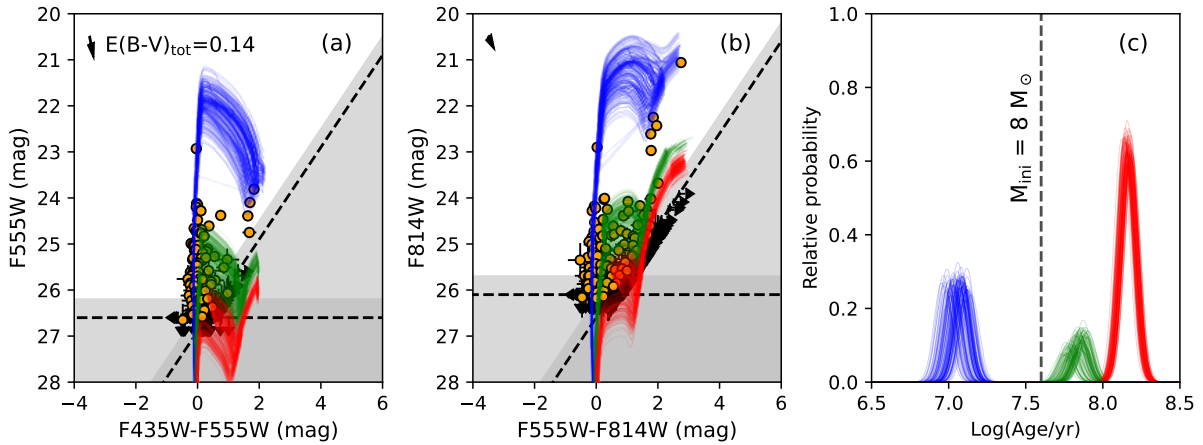
As shown in Fig. 1, there are a few H II regions at distances of 150–300 pc to the north and west of SN 2023ixf. Part of the northern H II region is also covered by our long-slit follow-up spectroscopy of SN 2023ixf with the Xinglong 2.16-m telescope (Fig. 1; Zhang et al. in preparation). Here we use one of the acquired spectra to investigate the ionized gas in the SN environment. This spectrum was observed on June 1st by the Beijing Faint Object Spectrograph and Camera (BFOSC) and G4+385LP grism (Fan et al. 2016). The wavelength range is from 3700 to 8800 and the exposure time is 1200 s. The spectrum of the H II region was extracted from the red-outlined area in Fig. 1, and data reduction was performed with the ASTRO-PLPY package<sup>3</sup>.

Figure 4 shows the extracted spectrum, from which a stellar continuum has been fit (with the PPXF package; Cappellari & Emsellem 2004; Cappellari 2017) and removed. Prominent nebular emission lines are apparent (such as H $\alpha$ , H $\beta$ , [N II]  $\lambda\lambda$  6548, 6583, [O I]  $\lambda\lambda$  6300, 6363, [O III]  $\lambda\lambda$  4959, 5007, and [S II]  $\lambda\lambda$  6716, 6731), and we measured their fluxes by fitting Gaussian profiles (Fig. 4b, c). With the O3N2 calibration of the strong-line diagnostics (Marino et al. 2013), we derived an oxygen abundance of  $12 + \log(\text{O}/\text{H}) = 8.37 \pm 0.18$  dex, which is lower than the solar value (8.69 dex;

<sup>3</sup> <https://pypi.org/project/astro-plpy>



**Figure 4.** (a) Continuum-subtracted spectrum of the nearby H II region to the north of SN 2023ixf (Fig. 1). The grey-shaded wavelength ranges are enlarged in panels (b) and (c), where the red and blue lines display the total and single Gaussian fits to the nebular emission lines, respectively.



**Figure 5.** (a, b) Color-magnitude diagrams of resolved stellar populations within 150 pc from SN 2023ixf (orange data points). The error bars reflect their  $1\sigma$  photometric uncertainties. The dashed lines show the 50 per cent detection limits, and the grey-shaded regions show where  $\leq 68$  per cent of the artificial stars can be successfully recovered. Model stellar populations with three age components are fitted to the data, and the (blue, green, and red) thin lines are stellar isochrones from 100 random realizations according to the stellar log-age and extinction distributions of the model populations. The arrows in the upper-left corners are total (Galactic + internal) reddening vectors for a standard extinction law with  $R_V = 3.1$ . (c) The star formation history in the vicinity of SN 2023ixf from 100 random realizations; the heights of the peaks are scaled to correspond to the weighting of each star formation epoch.

Asplund et al. 2009) by 0.32 dex (i.e. half-solar metallicity). We note however, the strong-line method could suffer from possible systematic uncertainties.

#### 4.2. Star formation history

In the immediate SN vicinity, there are no obvious signs of ongoing star formation on the HST or IRAC images (e.g. young stellar complexes, H $\alpha$  emission or dust IR emission; Fig. 1). In this area, the most recent star-forming activity may occur some time ago, after which star formation ceased or declined to very low levels. In order to recover the past star formation history, we analyzed the resolved stellar populations within  $\sim 150$  pc from SN 2023ixf based on their HST/ACS F435W/F555W/F814W photometry. In each band, we used only detections with signal-to-noise ratios larger than 5, and required their DOLPHOT sharpness parameter to be in the range of  $-0.5 < \text{SHARP} < 0.5$ , so that the selected sources have point-like morphologies. We also used randomly positioned artificial stars to estimate a detection limit and additional photometric uncertainties induced by source crowding and imperfect sky subtraction. A total of 362 stars are detected in the local environment of SN 2023ixf and their color-magnitude diagrams are displayed in Fig. 5.

We then fitted model stellar populations (based on the PARSEC v1.2S stellar evolutionary models; Bressan et al. 2012) to the data with a hierarchical Bayesian method, which was detailed in Maund & Ramirez-Ruiz (2016) and Sun et al. (2021) (see also Maund 2017, 2018; Sun et al. 2020a, 2022, 2023a,b). In brief, each model population has a Salpeter (1955) initial mass function, a 50 per cent (non-interacting) binary fraction, and a flat distribution of secondary-to-primary mass ratio. Stars of each population has Gaussian log-age and extinction distributions, and we assumed a small log-age dispersion of 0.05 dex and a small extinction dispersion of 0.05 mag. Prolonged star formation can be considered as the superposition of multiple stellar populations with different mean log-ages.

We used three model populations to fit the data and solve for their parameters with the dynamic nested sampling package DYNESTY (Speagle 2020). We derived a mean (host galaxy) extinction of  $A_V^{\text{host}} = 0.4$  mag, and mean log-ages of 7.07, 7.84 and 8.16 dex for the three age components (i.e. 12, 69, and 144 Myr). The derived star formation history and stellar isochrones corresponding to the three model populations are displayed in Fig. 5.

We note that the derived extinction is significantly larger than that for the SN itself (e.g. Smith et al. 2023). We argue that this is not unreasonable, since interstellar extinction often has significant spatial variation and the

progenitor of SN 2023ixf could have expelled the nearby dust with its intensive radiation and stellar wind. Liu et al. (private communications) performed an environmental analysis of SN 2023ixf based on integral-field-unit spectroscopy. With Balmer decrement they found a total reddening of  $E(B - V)_{\text{tot}} = 0.11 \pm 0.06$  mag for the ionized gas within 3 arcsec from SN 2023ixf. This corresponds to a host-galaxy extinction of  $A_V^{\text{host}} = 0.3 \pm 0.2$  mag, consistent with our results.

Assuming single-star evolution, the most recent star-forming burst corresponds to a SN progenitor mass of  $M_{\text{ini}} = 17\text{--}19 M_{\odot}$  (considering a conservative log-age uncertainty of 0.05 dex) and the earlier star formation epochs are too old to be consistent with a core-collapse SN. This result again suggests a relatively massive progenitor and is in agreement with the mass estimate derived from SED fitting (Section 3).

## 5. COMPARISON WITH PREVIOUS STUDIES

Pledger & Shara (2023) identified the progenitor of SN 2023ixf from the HST images and suggested it to be within the relatively low initial mass range of 8–10  $M_{\odot}$ . They noted the star may be subject to significant extinction, which would be difficult to estimate without the near- and mid-IR data.

Kilpatrick et al. (2023) also reported the detection of the progenitor of SN 2023ixf. With SED fitting, they derived a progenitor mass of only  $M_{\odot} = 11 M_{\odot}$ , which is significantly smaller than our result. This difference could be partly due to the stellar brightness variability. The HST observations were conducted at only one epoch, and it is difficult to estimate the phase-weighted average magnitudes in the optical bands. In order to account for this effect, we allowed the F675W and F814W model magnitudes to vary within 0.5 mag from the observed values, i.e. over a much larger range than the photometric uncertainties (Section 3). In fact, our best-fitting model SEDs predict brighter magnitudes in these two optical bands than the observed ones. In a test we found that the derived bolometric luminosity would be much smaller if we strictly required the model SEDs to match the observed F675W and F814W magnitudes within photometric uncertainties. This is consistent with the finding of Jencson et al. (2023) that the HST observations were timed near the bottom of the pulsation cycle. In addition, we have included the *JHK*-band photometry reported by Soraisam et al. (2023), while in Kilpatrick et al. (2023) the *JH*-band are detection limits. In our analysis we found the progenitor’s SED peaks near the *J* and *H* bands (Fig. 3), while their best-fitting model SED peaks at a slightly longer wavelength.



Jencson et al. (2023) derived a bolometric luminosity of  $\log(L/L_\odot) = 5.1 \pm 0.2$  dex and initial mass of  $M_\odot = 17 \pm 4 M_\odot$  for the progenitor of SN 2023ixf, which are roughly consistent with our results. Their analysis was performed by fitting the near-IR and mid-IR phase-weighted average magnitudes based on the GRAMS models with O-rich silicate dust. As we pointed out in Section 3, however, the prominent silicate bump is rarely under the Spitzer/IRAC [8.0] detection limit. When a more strict limit (e.g  $2\sigma$ ) is applied, O-model is incompatible with the observations. We prefer a C-rich dust chemical composition. We note that Jencson et al. (2023) derived a detection limit of [8.0] > 11.8 mag, significantly brighter than ours (14.95 mag). For comparison, the estimate of Kilpatrick et al. (2023) (their Table 2) corresponds to a more strict detection limit of [8.0] > 16.1 mag, assuming a nominal zero-point flux of Vega of 64.9 Jy. The different values may arise from our different photometry techniques.

Soraisam et al. (2023) accurately measured the progenitor’s pulsational period and estimated its *K*-band absolute magnitude with the period-luminosity relation. They converted the absolute magnitude to a bolometric luminosity of  $\log(L/L_\odot) = 5.2$ – $5.4$  dex and inferred an initial mass of  $20 \pm 4 M_\odot$ , both of which are slightly larger than ours. The period-luminosity relation they used was calibrated based on 255 RSGs in M31 (Soraisam et al. 2018). For the progenitor of SN 2023ixf, however, it is still unclear whether a RSG just before SN explosion would still follow the same period-luminosity relation as those at earlier evolutionary stages.

In summary, it is very challenging to derive accurate parameters for the progenitor of SN 2023ixf, due to its brightness variability, the uncertain circumstellar dust, and the poor understanding of the stellar evolutionary stage shortly before the explosion. The environmental analysis (Section 4) avoids these obstacles (although it has its own difficulties; see the discussion of Sun et al. 2021) and, as an independent analysis, has derived consistent results as our SED fitting (Section 3). We believe, therefore, that our conclusion should be reliable that SN 2023ixf has a relatively massive progenitor with an initial mass of  $M_{\text{ini}} = 16.2$ – $17.4 M_\odot$  (from SED fitting) or  $17$ – $19 M_\odot$  (from SN environment).

## 6. SUMMARY AND CONCLUSIONS

In this paper, we report a detailed analysis of the progenitor of the nearby Type II SN 2023ixf. Two independent analyses, based on direct progenitor detection in pre-explosion observations and an analysis of the SN environment, are used and they reach consistent results.

The progenitor of SN 2023ixf is significantly detected on the pre-explosion images acquired by HST in the F658N, F675W, and F814W bands and by Spitzer in the [3.6] and [4.5] bands. In agreement with previous studies, the mid-IR light curves exhibit significant variability without obvious color changes.

The progenitor’s SED is consistent with a RSG enshrouded by a dusty envelope. We modelled the SED by calculating the radiative transfer through dust; two different dust compositions were considered, i.e. C-rich pure graphite and O-rich pure silicate. Only the C-rich model seems consistent with observations and, assuming an effective temperature of  $T_{\text{eff}} \sim 3700$  K, the progenitor star has a bolometric luminosity of  $\log(L/L_\odot) = 5.11$  dex, corresponding to an initial mass of  $M_{\text{ini}} = 16.2$ – $17.4 M_\odot$ . The mass-loss rate is about  $1 \times 10^{-5} M_\odot/\text{yr}$ .

We also analyzed the environment of SN 2023ixf as another approach to understand its progenitor. A few H II regions are located at distances of 150–300 pc from the SN, and we derived a half-solar metallicity from strong nebular emission lines.

In the immediate SN vicinity (<150 pc) there are no obvious signs of ongoing star formation. We derived the star formation history based on the resolved stellar populations. While most star-forming bursts are too old to be consistent with a core-collapse SN, the most recent one occurred 12 Myr ago, corresponding to an initial mass of  $M_{\text{ini}} = 17$ – $19 M_\odot$  for the progenitor of SN 2023ixf, assuming single-star evolution.

In summary, the progenitor of SN 2023ixf is among the most massive ones that have been directly probed for Type II SNe. For such a massive progenitor, the powerful stellar wind likely drives significant mass loss and results in a low-mass H envelope, which could explain the continuous linear decay of the light curve out to 50 days after explosion (Bianciardi et al. 2023). It remains to be explored whether binary evolution plays any role for the progenitor of SN 2023ixf, although currently no obvious signs for a companion star have been discovered.

## 7. ACKNOWLEDGMENTS

ZXN acknowledges the helpful discussions with Dr. Shu Wang, and NCS is grateful to Dr. Chenxu Liu for providing the extinction value estimated with itegral-field-unit spectroscopic data. NCS’s research is funded by the NSFC grant No. 12261141690. The research of JRM is supported by the STFC consolidated grant ST/V000853/1. JFL acknowledges support from the NSFC through grant Nos. 11988101 and 11933004, and support from the New Cornerstone Science Foundation

through the New Cornerstone Investigator Program and the XPLOER PRIZE. This work is based on observa-

tions made with the Hubble Space Telescope and the Spitzer Space Telescope.

## REFERENCES

- Asplund, M., Grevesse, N., Sauval, A. J., & Scott, P. 2009, *ARA&A*, 47, 481, doi: [10.1146/annurev.astro.46.060407.145222](https://doi.org/10.1146/annurev.astro.46.060407.145222)
- Beasor, E. R., & Davies, B. 2016, *MNRAS*, 463, 1269, doi: [10.1093/mnras/stw2054](https://doi.org/10.1093/mnras/stw2054)
- Beasor, E. R., Davies, B., Smith, N., et al. 2020, *MNRAS*, 492, 5994, doi: [10.1093/mnras/staa255](https://doi.org/10.1093/mnras/staa255)
- . 2023, *MNRAS*, 524, 2460, doi: [10.1093/mnras/stad1818](https://doi.org/10.1093/mnras/stad1818)
- Bianciardi, G., Ciccarelli A., M., Conzo, G., et al. 2023, arXiv e-prints, arXiv:2307.05612, doi: [10.48550/arXiv.2307.05612](https://doi.org/10.48550/arXiv.2307.05612)
- Bressan, A., Marigo, P., Girardi, L., et al. 2012, *MNRAS*, 427, 127, doi: [10.1111/j.1365-2966.2012.21948.x](https://doi.org/10.1111/j.1365-2966.2012.21948.x)
- Cappellari, M. 2017, *MNRAS*, 466, 798, doi: [10.1093/mnras/stw3020](https://doi.org/10.1093/mnras/stw3020)
- Cappellari, M., & Emsellem, E. 2004, *PASP*, 116, 138, doi: [10.1086/381875](https://doi.org/10.1086/381875)
- Cardelli, J. A., Clayton, G. C., & Mathis, J. S. 1989, *ApJ*, 345, 245, doi: [10.1086/167900](https://doi.org/10.1086/167900)
- Davies, B., & Beasor, E. R. 2018, *MNRAS*, 474, 2116, doi: [10.1093/mnras/stx2734](https://doi.org/10.1093/mnras/stx2734)
- Davies, B., Kudritzki, R.-P., Plez, B., et al. 2013, *ApJ*, 767, 3, doi: [10.1088/0004-637X/767/1/3](https://doi.org/10.1088/0004-637X/767/1/3)
- de Jager, C., Nieuwenhuijzen, H., & van der Hucht, K. A. 1988, *A&AS*, 72, 259
- Dolphin, A. E. 2000, *PASP*, 112, 1383, doi: [10.1086/316630](https://doi.org/10.1086/316630)
- Draine, B. T., & Lee, H. M. 1984, *ApJ*, 285, 89, doi: [10.1086/162480](https://doi.org/10.1086/162480)
- Eldridge, J. J., Fraser, M., Smartt, S. J., Maund, J. R., & Crockett, R. M. 2013, *MNRAS*, 436, 774, doi: [10.1093/mnras/stt1612](https://doi.org/10.1093/mnras/stt1612)
- Elias-Rosa, N., Van Dyk, S. D., Li, W., et al. 2010, *ApJL*, 714, L254, doi: [10.1088/2041-8205/714/2/L254](https://doi.org/10.1088/2041-8205/714/2/L254)
- Fan, Z., Wang, H., Jiang, X., et al. 2016, *PASP*, 128, 115005, doi: [10.1088/1538-3873/128/969/115005](https://doi.org/10.1088/1538-3873/128/969/115005)
- Fang, Q., Maeda, K., Kuncarayakti, H., Sun, F., & Gal-Yam, A. 2019, *Nature Astronomy*, 3, 434, doi: [10.1038/s41550-019-0710-6](https://doi.org/10.1038/s41550-019-0710-6)
- Faran, T., Poznanski, D., Filippenko, A. V., et al. 2014, *MNRAS*, 445, 554, doi: [10.1093/mnras/stu1760](https://doi.org/10.1093/mnras/stu1760)
- Gonzaga, S., Hack, W., Fruchter, A., & Mack, J. 2012, *The DrizzlePac Handbook*
- Groh, J. H., Meynet, G., & Ekström, S. 2013, *A&A*, 550, L7, doi: [10.1051/0004-6361/201220741](https://doi.org/10.1051/0004-6361/201220741)
- Gustafsson, B., Edvardsson, B., Eriksson, K., et al. 2008, *A&A*, 486, 951, doi: [10.1051/0004-6361:200809724](https://doi.org/10.1051/0004-6361:200809724)
- Hiramatsu, D., Tsuna, D., Berger, E., et al. 2023, arXiv e-prints, arXiv:2307.03165, doi: [10.48550/arXiv.2307.03165](https://doi.org/10.48550/arXiv.2307.03165)
- Itagaki, K. 2023, *Transient Name Server Discovery Report*, 2023-1158, 1
- Jacobson-Galan, W. V., Dessart, L., Margutti, R., et al. 2023, arXiv e-prints, arXiv:2306.04721, doi: [10.48550/arXiv.2306.04721](https://doi.org/10.48550/arXiv.2306.04721)
- Jencson, J. E., Pearson, J., Beasor, E. R., et al. 2023, arXiv e-prints, arXiv:2306.08678, doi: [10.48550/arXiv.2306.08678](https://doi.org/10.48550/arXiv.2306.08678)
- Kilpatrick, C. D., Foley, R. J., Jacobson-Galán, W. V., et al. 2023, *ApJL*, 952, L23, doi: [10.3847/2041-8213/ace4ca](https://doi.org/10.3847/2041-8213/ace4ca)
- Kochanek, C. S., Szczygieł, D. M., & Stanek, K. Z. 2012, *ApJ*, 758, 142, doi: [10.1088/0004-637X/758/2/142](https://doi.org/10.1088/0004-637X/758/2/142)
- Lundquist, M., O’Meara, J., & Walawender, J. 2023, *Transient Name Server AstroNote*, 160, 1
- Marino, R. A., Rosales-Ortega, F. F., Sánchez, S. F., et al. 2013, *A&A*, 559, A114, doi: [10.1051/0004-6361/201321956](https://doi.org/10.1051/0004-6361/201321956)
- Massey, P., Plez, B., Levesque, E. M., et al. 2005, *ApJ*, 634, 1286, doi: [10.1086/497065](https://doi.org/10.1086/497065)
- Mathis, J. S., Rumpl, W., & Nordsieck, K. H. 1977, *ApJ*, 217, 425, doi: [10.1086/155591](https://doi.org/10.1086/155591)
- Maund, J. R. 2017, *MNRAS*, 469, 2202, doi: [10.1093/mnras/stx879](https://doi.org/10.1093/mnras/stx879)
- . 2018, *MNRAS*, 476, 2629, doi: [10.1093/mnras/sty093](https://doi.org/10.1093/mnras/sty093)
- Maund, J. R., Fraser, M., Reilly, E., Ergon, M., & Mattila, S. 2015, *MNRAS*, 447, 3207, doi: [10.1093/mnras/stu2658](https://doi.org/10.1093/mnras/stu2658)
- Maund, J. R., & Ramirez-Ruiz, E. 2016, *MNRAS*, 456, 3175, doi: [10.1093/mnras/stv2760](https://doi.org/10.1093/mnras/stv2760)
- Maund, J. R., & Smartt, S. J. 2009, *Science*, 324, 486, doi: [10.1126/science.1170198](https://doi.org/10.1126/science.1170198)
- Maund, J. R., Smartt, S. J., & Danziger, I. J. 2005, *MNRAS*, 364, L33, doi: [10.1111/j.1745-3933.2005.00100.x](https://doi.org/10.1111/j.1745-3933.2005.00100.x)
- Maund, J. R., Smartt, S. J., Kudritzki, R. P., Podsiadlowski, P., & Gilmore, G. F. 2004, *Nature*, 427, 129, doi: [10.1038/nature02161](https://doi.org/10.1038/nature02161)
- Pledger, J. L., & Shara, M. M. 2023, arXiv e-prints, arXiv:2305.14447, doi: [10.48550/arXiv.2305.14447](https://doi.org/10.48550/arXiv.2305.14447)
- Pozzo, M., Meikle, W. P. S., Fassia, A., et al. 2004, *MNRAS*, 352, 457, doi: [10.1111/j.1365-2966.2004.07951.x](https://doi.org/10.1111/j.1365-2966.2004.07951.x)

- Riess, A. G., Yuan, W., Macri, L. M., et al. 2022, *ApJL*, 934, L7, doi: [10.3847/2041-8213/ac5c5b](https://doi.org/10.3847/2041-8213/ac5c5b)
- Rui, L., Wang, X., Mo, J., et al. 2019, *MNRAS*, 485, 1990, doi: [10.1093/mnras/stz503](https://doi.org/10.1093/mnras/stz503)
- Salpeter, E. E. 1955, *ApJ*, 121, 161, doi: [10.1086/145971](https://doi.org/10.1086/145971)
- Sarangi, A., Dwek, E., & Arendt, R. G. 2018, *ApJ*, 859, 66, doi: [10.3847/1538-4357/aabfc3](https://doi.org/10.3847/1538-4357/aabfc3)
- Schechter, P. L., Mateo, M., & Saha, A. 1993, *PASP*, 105, 1342, doi: [10.1086/133316](https://doi.org/10.1086/133316)
- Schlafly, E. F., & Finkbeiner, D. P. 2011, *ApJ*, 737, 103, doi: [10.1088/0004-637X/737/2/103](https://doi.org/10.1088/0004-637X/737/2/103)
- Smartt, S. J. 2009, *ARA&A*, 47, 63, doi: [10.1146/annurev-astro-082708-101737](https://doi.org/10.1146/annurev-astro-082708-101737)
- . 2015, *PASA*, 32, e016, doi: [10.1017/pasa.2015.17](https://doi.org/10.1017/pasa.2015.17)
- Smartt, S. J., Maund, J. R., Hendry, M. A., et al. 2004, *Science*, 303, 499, doi: [10.1126/science.1092967](https://doi.org/10.1126/science.1092967)
- Smith, N., Pearson, J., Sand, D. J., et al. 2023, arXiv e-prints, arXiv:2306.07964, doi: [10.48550/arXiv.2306.07964](https://doi.org/10.48550/arXiv.2306.07964)
- Soraisam, M. D., Bildsten, L., Drout, M. R., et al. 2018, *ApJ*, 859, 73, doi: [10.3847/1538-4357/aabc59](https://doi.org/10.3847/1538-4357/aabc59)
- Soraisam, M. D., Szalai, T., Van Dyk, S. D., et al. 2023, arXiv e-prints, arXiv:2306.10783, doi: [10.48550/arXiv.2306.10783](https://doi.org/10.48550/arXiv.2306.10783)
- Speagle, J. S. 2020, *MNRAS*, 493, 3132, doi: [10.1093/mnras/staa278](https://doi.org/10.1093/mnras/staa278)
- Sukhbold, T., Ertl, T., Woosley, S. E., Brown, J. M., & Janka, H. T. 2016, *ApJ*, 821, 38, doi: [10.3847/0004-637X/821/1/38](https://doi.org/10.3847/0004-637X/821/1/38)
- Sun, N.-C., Maund, J. R., & Crowther, P. A. 2020a, *MNRAS*, 497, 5118, doi: [10.1093/mnras/staa2277](https://doi.org/10.1093/mnras/staa2277)
- . 2023a, *MNRAS*, 521, 2860, doi: [10.1093/mnras/stad690](https://doi.org/10.1093/mnras/stad690)
- Sun, N.-C., Maund, J. R., Crowther, P. A., Fang, X., & Zapartas, E. 2021, *MNRAS*, 504, 2253, doi: [10.1093/mnras/stab994](https://doi.org/10.1093/mnras/stab994)
- Sun, N.-C., Maund, J. R., Crowther, P. A., et al. 2022, *MNRAS*, 510, 3701, doi: [10.1093/mnras/stab3768](https://doi.org/10.1093/mnras/stab3768)
- Sun, N.-C., Maund, J. R., Hirai, R., Crowther, P. A., & Podsiadlowski, P. 2020b, *MNRAS*, 491, 6000, doi: [10.1093/mnras/stz3431](https://doi.org/10.1093/mnras/stz3431)
- Sun, N.-C., Maund, J. R., Shao, Y., & Janiak, I. A. 2023b, *MNRAS*, 519, 3785, doi: [10.1093/mnras/stac3773](https://doi.org/10.1093/mnras/stac3773)
- Swartz, D. A., Wheeler, J. C., & Harkness, R. P. 1991, *ApJ*, 374, 266, doi: [10.1086/170115](https://doi.org/10.1086/170115)
- Teja, R. S., Singh, A., Dutta, A., et al. 2023, arXiv e-prints, arXiv:2306.10284, doi: [10.48550/arXiv.2306.10284](https://doi.org/10.48550/arXiv.2306.10284)
- Van Dyk, S. D., Zheng, W., Maund, J. R., et al. 2019, *ApJ*, 875, 136, doi: [10.3847/1538-4357/ab1136](https://doi.org/10.3847/1538-4357/ab1136)
- van Loon, J. T., Cioni, M. R. L., Zijlstra, A. A., & Loup, C. 2005a, *A&A*, 438, 273, doi: [10.1051/0004-6361:20042555](https://doi.org/10.1051/0004-6361:20042555)
- van Loon, J. T., Marshall, J. R., & Zijlstra, A. A. 2005b, *A&A*, 442, 597, doi: [10.1051/0004-6361:20053528](https://doi.org/10.1051/0004-6361:20053528)
- Vasylyev, S. S., Yang, Y., Filippenko, A. V., et al. 2023, arXiv e-prints, arXiv:2307.01268, doi: [10.48550/arXiv.2307.01268](https://doi.org/10.48550/arXiv.2307.01268)
- Walmswell, J. J., & Eldridge, J. J. 2012, *MNRAS*, 419, 2054, doi: [10.1111/j.1365-2966.2011.19860.x](https://doi.org/10.1111/j.1365-2966.2011.19860.x)
- Yamanaka, M., Fujii, M., & Nagayama, T. 2023, arXiv e-prints, arXiv:2306.00263, doi: [10.48550/arXiv.2306.00263](https://doi.org/10.48550/arXiv.2306.00263)